LUND UNIVERSITY

High-repetition-rate, hard x-ray radiation from a laser-produced plasma: Photon yield and application considerations

Sjögren, Anders; Harbst, Michael; Wahlström, Claes-Göran; Svanberg, Sune; Olsson, C

[Link to publication]

Total number of authors:
5

High-repetition-rate, hard x-ray radiation from a laser-produced plasma: Photon yield and application considerations

A. Sjögren, M. Harbst,[a] C.-G. Wahlström, and S. Svanberg
Department of Physics, Lund Institute of Technology, P. O. Box 118, SE-221 00 Lund, Sweden

C. Olsson
Department of Diagnostic Radiology, Lund University Hospital, SE-221 85 Lund, Sweden

We present an experimental study of hard x rays produced in laser-produced plasmas. The laser used is a 1 kHz system, delivering 0.7 mJ for 25 fs onto a solid target. The x-ray spectrum was measured with calibrated germanium detectors, allowing a very good estimate of the absolute number of photons emitted from the plasma over a wide energy range; from 7 keV to 0.5 MeV. Assuming a bi-Maxwellian electron distribution with temperatures of 4.5 and 63 keV, theoretical calculations support the experimental findings. The imaging characteristics of the x-ray source were investigated experimentally employing image plates and theoretically based on the electron distribution. © 2003 American Institute of Physics. [DOI: 10.1063/1.1544054]

I. INTRODUCTION

Since the appearance of titanium-sapphire-based femtosecond lasers with relatively high repetition rates ($\geq$10 Hz), they have been incorporated into the science of laser-produced hard x rays. The laser pulses are usually focused onto a solid target of a high-Z material where they generate a hot plasma which radiates mainly bremsstrahlung radiation.[1] This x-ray emission of ultrashort duration, broad spectral range, and high brightness, is currently of considerable interest for various applications. For example, already 10 years ago some results of medical imaging with laser-produced hard x rays were reported.[2]

The average output power of this type of laser is typically 1–10 W, irrespective of the repetition rate. With 10 Hz systems the pulse energies lay in the range 0.1–1 J, and with 1 kHz systems two orders of magnitude lower. The lasers tend to decrease in size with decreasing pulse energy, i.e., increasing repetition rate. From the user's point of view the amount and quality of the x rays are important. The question is whether the average x-ray power and the x-ray spectrum with lower energy pulses compare to the those generated by more energetic laser pulses. Most investigations of the radiation above 10 keV have dealt with the x-ray yield and energy spectrum produced with low-repetition-rate laser systems;[3–8] only a few have considered laser systems with repetition rates equal to, or higher than, 1 kHz.[9]

Typically, in experiments producing hard x rays, a parameter such as the laser pulse energy is varied. In the lower energy range, below 50 keV, the detection techniques available include photon counting using a charge coupled device (CCD),[9] or a CCD in combination with a crystal diffracting x rays.[10,11] Detectors that can be used above 100 keV include x-ray diodes,[12] scintillation detectors,[13–15] thermoluminescence detectors,[3] and germanium (Ge) detectors.[16,17] The lat-

ter can easily detect photons with energies of several mega-electron-volts. Since many x-ray detectors have been developed for the nuclear science community, they have been adapted to the more or less constant x-ray fluxes which are common in this field.

Laser-generated x-ray pulses, however, are generally very of short duration (<50 ps). Detection and measurement of the x-ray spectrum can be accomplished by single-photon-sensitive detectors, but in an environment where, figuratively speaking, "all the photons come at the same time," it is difficult to suppress pileup, i.e., the simultaneous detection of several photons. Since no more than one x-ray photon can be correctly detected per laser pulse, the data acquisition time can be very long with a 10 Hz laser.[17] However, with higher repetition-rate lasers, the technique becomes more attractive. Alternatively, energy-dispersive optics can be utilized, such as diffracting crystals, but these have their own drawbacks at high photon energies.

This article describes an experimental investigation of the x-ray emission from a laser-produced plasma. It is an extension of earlier work with a 10 Hz TW laser performed at the High Power Laser Facility, which is a part of the Lund Laser Center.[11,17–20] The x rays were produced by obliquely focusing p-polarized laser pulses from a 1 kHz laser system onto a rotating tantalum target, whereby a hot, nonequilibrium plasma was produced. The prepulse level was kept low in order to minimize the formation of an early preplasma. The main pulse therefore interacts with a plasma with a sharp density profile, and various plasma heating mechanisms, including resonance and vacuum heating, become important.[21–24] Some electrons penetrate into the surrounding cold metal and bremsstrahlung and characteristic radiation are emitted. We measured a large part of the radiation spectrum in absolute terms through the use of two Ge detectors.

The measured spectra were used to reconstruct the plasma emission spectrum with estimates of the isotropic

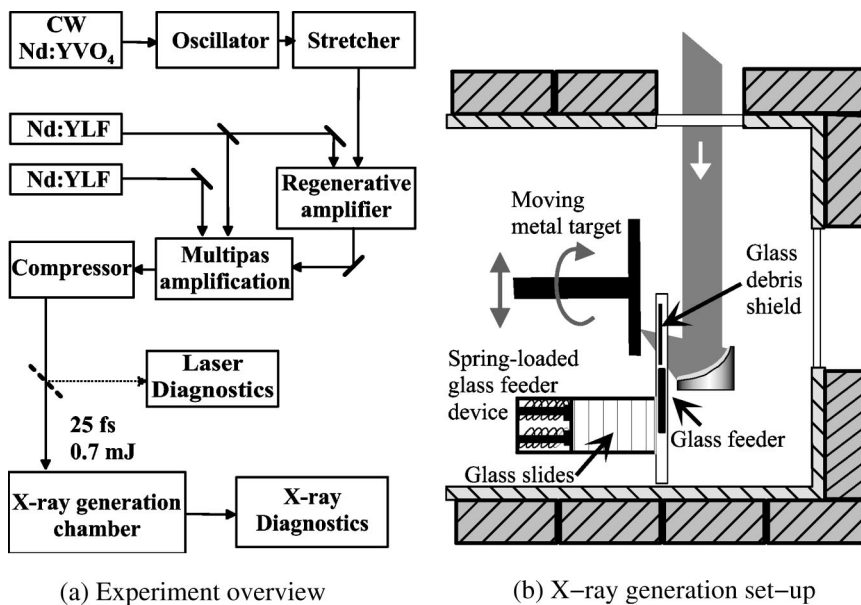[a]Electronic mail: michael.harbst@fysik.lth.se

FIG. 1. (a) Schematic diagram of the kilohertz laser and the x-ray generation and detection setup. (b) The setup for x-ray generation in detail showing a section of the aluminum vacuum chamber and the lead bricks surrounding it. The laser beam is 25 mm *i* diameter and is focused by an *f*/1 mirror, through a thin glass plate, onto the rotating and translated solid target. The cassette and feeder which permit the shielding glass to be changed during operation are also shown.

(a) Experiment overview

(b) X−ray generation set−up

spectral radiant intensity distribution, $(\mathrm{W\,sr^{-1}\,keV^{-1}})$. It is a difficult task to assess the true emission spectrum, mainly due to Compton scattering and pileup in the detectors. Rather than trying to reconstruct the emitted spectrum directly from the measured data, we started with a theoretical emission spectrum, which was "propagated" to the detectors, using simple models for Compton scattering and pileup, and we then compared the detector spectra with the simulated ones. The theoretical emission spectrum was generated by an electron distribution parameterized by several Maxwell distributions. Very good agreement was achieved between the simulation and the experimental spectra with a dual-temperature electron distribution.

In Secs. II and III the kilohertz laser and the setup for laser-produced x rays are described. Thereafter follows a section about the detectors and certain detection techniques. Section V deals with the theoretical model used to find the closest match between the theoretical emission spectrum and the measured spectra. Sections VI and VII contain the results from this experiment and their analysis. Finally, the results and the potential of this x-ray source are discussed in the conclusions.

II. THE LASER

The laser used in the experiment is a titanium–sapphire system based on the chirped-pulse amplification technique [Fig. 1(a)]. It consists of a broadband, femtosecond oscillator, a grating stretcher, a regenerative amplifier followed by two "butterfly" type amplifiers, and a grating compressor. Two frequency-doubled Nd:YLF lasers pump the system with up to 40 W of green light. In this experiment, the laser delivered pulses with 0.7 mJ energy and 25 fs pulse duration (20% day-to-day variation) at 1 kHz. The spatial mode is roughly Airy shaped with the first minimum diameter of 24 mm. The laser is equipped with an extra Pockels cell after the regenerative amplifier, which enhances the pre- to main pulse energy ratio to approximately 10^{-4}. The train of prepulses has a pulse-to-pulse separation of 10 ns.

During the experiment, several laser pulse properties were regularly measured, usually every time the target was changed. The diagnostic equipment is employed through the use of flip-in mirrors in the path between the compressor and the experimental vacuum chamber. A second-order autocorrelator monitors the pulse duration. The light path to the autocorrelator is designed so as to contain the same amount of glass, approximately 6 mm fused silica, as the path to the focus in the experimental chamber. The pulse duration at the focus is therefore the same as the measured pulse duration. A spectrometer was used to measure the 70 nm wide laser spectrum. The prepulse contrast was assessed using of two fast photodiodes and a 1 GHz sample rate oscilloscope. One of the diodes monitors the main pulse and controls the trigger to the oscilloscope, while the other measures the prepulse level. The setup was calibrated with a procedure employing neutral-density filters. The spatial energy distribution was assessed via visual inspection of the mode on fluorescent paper and "burn paper" (Kodak Linagraph direct print).

III. THE X-RAY GENERATION SETUP

The experimental setup is schematically illustrated in Fig. 1(b). The horizontally polarized laser pulse propagates perpendicularly through a 6 mm fused silica window to enter the vacuum chamber, kept at about 10^3 Pa, and the x rays exit through a large 15 cm diameter and 180-μm-thick plastic window. The vacuum chamber is otherwise enclosed in 5-cm-thick lead. The laser pulse is focused by a 25 mm diameter, f/1, off-axis parabolic mirror coated with gold (Janos A8037-116). The mirror reflects the light back at 60° to the incoming beam, giving an angle of incidence of 30° at the target; close to the optimum.[23,25–27] The converging light passes through a 110-μm-thick glass plate (optical microscopy cover plate) and focuses onto the solid target. The parabolic mirror is aligned in air by gradually lowering the laser pulse energy while adjusting the mirror mount and maintaining a visible spark in the focus.

The glass plate, together with aluminum foil, shield the mirror from the debris that is produced in the interaction between the laser pulse and the target material. It appears that the debris emitted by target consists primarily of heavy, molten particles that stick to the first surface they strike. Blocking the direct path from the focus to the mirror is therefore sufficient to keep the mirror clean during experiments. However, the glass plate becomes dirty and the light transmission diminishes over time. The amount of debris can vary considerably in different experiments but the glass cover is replaced every 10 min on average (after $\sim 10^5$ pulses). This can be compared with a replacement rate of once every minute (after $\lesssim 10^3$ pulses) when employing our more powerful 10 Hz laser system.[28] Shield replacement is performed remotely without opening the chamber by a direct current motor that inserts a new glass plate from a specially designed glass feeder cassette.

Throughout this study the target material used was tantalum. The targets are 50 mm diameter disks, 2 mm thick, welded onto a steel base that fits on an adjustable mount. This mount is fastened centrally to a steel axis, which in turn is held in place by two ball bearings and connected to a stepping motor with 180 steps per turn. The whole gear is fitted via a piezocontrolled mount to two perpendicularly mounted motorized translators. The translation axes are along the axis of rotation and perpendicularly to it in the horizontal plane.

The tantalum targets are turned and polished before use, until they have the appearance of foggy mirrors. When studied in a microscope they reveal a very flat surface with many shallow scratches, ~ 1 μm deep and a few microns long. As the depth of the laser focus is only of the order of a few microns the target must be accurately positioned. However, the rotating target wobbles slightly due to mechanical imperfections. In order to reduce the deviation from the focus that occurs when the target is moved, a position-sensitive "finger" is pressed against the target surface a few millimetres below the laser focus. The target position, along its rotation axis, acts through the finger and generates a voltage in a receiver (Mμ-checker, Mitutoyo). It produces the input signal for a stabilization routine that regulates the voltage to the piezocontrolled mount mentioned earlier, which adjusts the target position along its axis of rotation. With this system, a well-turned and polished tantalum target can be held in focus within ± 2 μm over one rotation.

As the laser fires onto the target other software controls the motion of the target. It is rotated and translated sideways simultaneously in order to position the consecutive foci on a line that starts at the edge of the target and spirals in towards the center. Thus, every laser pulse focuses on a fresh, polished part of the target. The number of laser pulses fired and the desired focus separation are used to calculate the speed of rotation and the horizontal translation in real time. The software counts the laser pulses and reads the current horizontal position, then it regulates the output signals that control the target rotation and translation with a proportional-integrating-differentiating algorithm. In practice, this control system allows the foci to be separated by only 30 μm without running the risk of overlapping. With the laser operating
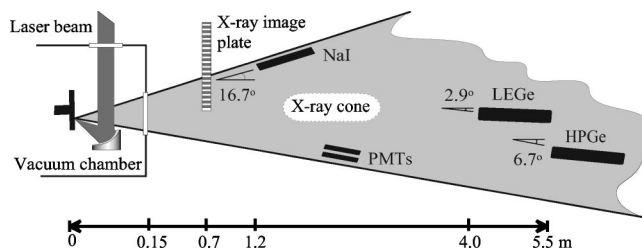

FIG. 2. The irradiated tantalum target with the laser-produced plasma is seen on the left. The x rays are emitted more or less isotropically, but only a cone of x rays will leave the vacuum chamber through its thin plastic window, as indicated. The lead bricks that shield the image plate and the Ge detectors have been omitted for clarity. The image plate, and its shield, block the path to the NaI detector but are only present when recording radiographs.

at 1 kHz a tantalum target lasts for about 35 min with such an interfocus separation, after which it must be replaced. The diameter of the craters formed by the laser pulses is about 7 μm, ten times smaller than with pulses from our 10 Hz laser (those laser pulses are of similar duration but contain 10^2-10^3 times more energy).[28] The focus separation is consequently limited by the accuracy of the motor control, not the crater size. The target lifetime could thus be extended by further decreasing the separation. It is worth mentioning that there are widely different ways of increasing the lifetime of the target, for example by using renewable liquid-metal jets or a metal-wire as targets.[29–31]

IV. X-RAY DETECTION

In the present experiment several detectors were utilized in order to monitor different x-ray radiation parameters. The time averaged flux of x rays was measured, as well as the pulse-to-pulse variation in x-ray intensity. The most important detectors were two Ge detectors which both sampled the x-ray spectral intensity. The imaging properties of the emitted radiation is assessed by recording radiographs on x-ray image plates. The geometry used and the positioning of the different detectors are illustrated schematically in Fig. 2.

Two scintillator-coupled photomultiplier tubes (PMTs) (Hamamatsu PMT R5600U) were used to monitor the average flux of x rays (Fig. 2). One scintillator was shielded by ~ 1 mm copper foil, making the detector less sensitive to low-energy x rays. The scintillating material (LG-9 TAR, Schott Fibre Optics Inc., USA) used has a slow decay (~ 1 ms) and did not recover between the x-ray bursts. The use of these detectors is essential when moving the target into the laser focus, by optimizing the average x-ray flux.

A NaI scintillator-coupled PMT (Scionix 51B51/2) was used to assess the integrated x-ray spectrum (Fig. 2). It is fast (although slower than a Ge detector) and sampled every individual x-ray burst, integrating the x-ray energy from about 20 keV and upwards; the lower energies were blocked by the 2-mm-thick aluminum casing. Assuming isotropic emission from the plasma the signal from this detector is proportional to the emitted x-ray energy. The detector was placed 1.2 m from the laser-produced plasma in order to avoid saturation. The amplified output signal was fed to a discriminator logic device (ORTEC Timing SCA 420A) with a user-defined win-

dow of voltages. The discriminator, in turn, controls a pulse counter and an electronic gate, referred to below as the intensity gate. The pulse counter merely registers the x-ray bursts which are not discriminated; a number which is useful for pileup analysis, as discussed later.

It is interesting to compare the Ge detector setup in this experiment, illustrated in Fig. 2, with the one used by Tillman *et al.* in 1997.[17] The distances between the x-ray source and the detectors were much larger in their experiments because of the higher x-ray intensity that was generated. The two germanium detectors shown in Fig. 2 are equipped with liquid-nitrogen-filled cryostats. The standard-electrode coaxial germanium (HPGe) detector (Canberra GC1819), with a 500-μm-thick aluminum window, is most sensitive to x-ray radiation in the region from 50 keV and upwards to several mega-electron-volts. The low-energy germanium (LEGe) detector (Canberra GL0210P), with a 50-μm-thick beryllium window, is most sensitive in the range from 5 keV up to a few hundred kilo-electron-volts. The lower and upper energy limits derive from the detector window and the germanium crystal design, respectively. However, on the way to the detectors, the x rays pass through the debris-shielding glass plate, the plastic window at the air-vacuum interface and several meters of air, which limits the lowest detectable energy to about 7 keV due to absorption. The LEGe crystal is 10 mm thick, while the HPGe crystal thickness, because of its special design, varies between roughly 3 and 6 cm. The detector design affords the LEGe detector its the superior energy resolution (the energy width detected from a monochromatic source): <0.2 keV below 10 keV and <0.5 keV above 100 keV. The HPGe resolution is <1 keV below 150 keV and <4 keV below 1.5 MeV.

The Ge detectors must be supplied with a low x-ray flux so as to avoid addition of the energies of consecutive photons in the detector. The only obvious parameter in this experiment that can be varied to reduce the flux is the solid angle subtended by the plasma at the detector. The detectors are placed in lead shielding, with a small hole in one lead brick through which the x rays can enter the detector. The solid angle is thus determined by the size of this lead aperture and its distance from the plasma. Furthermore, since the lead brick is 5 cm thick and the hole is of the order of a few millimeters, the acceptance angle for the detector is very small. Due to the high intensity of the x-ray burst, the detectors must be placed far from the x-ray source, even if the lead apertures are small; further reducing the solid angle. The detectors are connected to amplifiers that transmit triangle-shaped voltage pulses, 6 μs long, via a synchronization gate to two computer-based multichannel analyzers (MCAs). The pulse height, which determines the photon energy, is sampled by the MCAs and a spectrum forms when many events have been registered. The energy scale in the MCA is manually calibrated with radionuclide samples. The synchronization gate opens only for events that coincide with the laser pulses and thus blocks almost all events that are generated by the ambient background, including cosmic radiation. The gate is controlled by the laser and it is open for about 40 μs, the time during which plasma-generated x rays are expected to reach the detector. However, a significant amount of x-ray
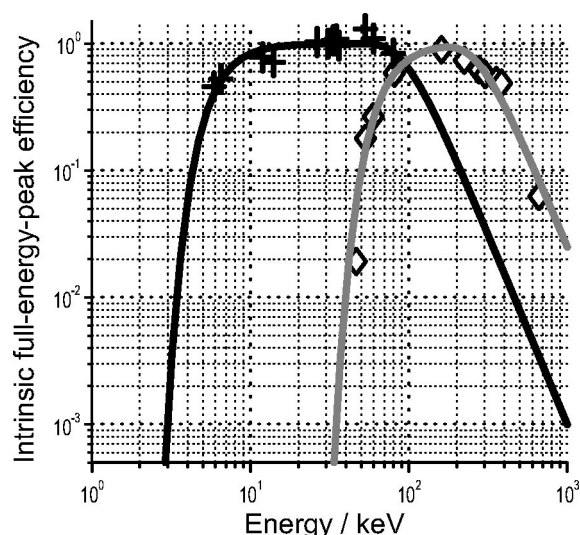

FIG. 3. The measured intrinsic full-energy-peak efficiency of the two germanium detectors. The measured efficiencies are indicated by + (LEGe) and ◇ (HPGe). The interpolation curves for the LEGe and HPGe detectors are shown in black and gray, respectively.

photons are promptly scattered from the surrounding materials towards the detectors. The presence of this background constitutes a serious threat (see the pileup discussion later) and must be minimized. The level of background and scattered x rays was measured by blocking the direct paths from the laser-plasma source to the detectors with steel and lead but leaving all indirect paths to the detector open. The x-ray block was placed about one meter from the x-ray source, leaving at least 3 m of air to the detectors. The experiment was, in all other respects, performed as usual and the acquired spectra reveal the amount of background radiation recorded. It was found that by shielding the detectors from scattered radiation and using the synchronization gate, the background was totally negligible.

The acquired x-ray spectra can be used to reconstruct the spectrum of the emitted x rays from the laser plasma. The process of doing this is thoroughly discussed in the following section. In calculating the emitted spectrum, the solid angle, the absorption, and the intrinsic, full-energy-peak efficiency of the detector are considered, as well as the effect of Compton scattering and pileup. Air absorption is significant below 20 keV. This absorption and the absorption in the glass plate and the plastic window at the vacuum-air interface are calculated with the use of the National Institute of Standards and Technology (NIST) databases.[32] The transmission curves for the glass and the plastic window were experimentally verified at a few energies using radionuclide samples. The measured and NIST transmissions agree within 10%. The intrinsic, full-energy-peak efficiency is the probability of detecting the correct energy of a photon that hits the detector. The efficiencies were estimated for both detectors using radionuclide samples with calibrated activity, and the results are presented in Fig. 3. The efficiency data are inter- and extrapolated using a physical model incorporating the product of a transmission function, representing the detector window, and an absorption function representing the absorption in the germanium crystal.

The derived laser-plasma emission spectra contain additional uncertainties besides the material transmissions and detector efficiencies. Germanium detectors are not perfect detectors, in the sense that every photon that enters the crystal is detected. Some photons, especially those with energies above a few tens of kilo-electron-volts, will be Compton scattered and deposit only a part of their energy, before leaving the detector. Such events contribute to a background which is most apparent at the lower energies in the spectrum. The effect of Compton scattering is very obvious in this experiment because photons with low energies will not reach the detectors (<7 keV for the LEGe and <40 keV for the HPGe). In spite of this, the acquired raw data spectra show clear tails of events in the low-energy regions. These are generated through Compton scattering.

The Ge detectors have a high readout rate, but photons that arrive within a few microseconds of each other will be counted as one event. The recorded energy will thus be the sum of the photon energies, an effect called ''pileup.'' This can be avoided by exposing the detectors to a sufficiently low x-ray flux. Typically, this corresponds to the probability of recording an event being below 10% in a single x-ray burst. However, with laser-produced plasmas this requirement is not sufficient. The x-ray generation process is extremely sensitive to fluctuations in the laser intensity and of the target position, which lead to large fluctuations in the x-ray yield. Suppose that the lead aperture in front of the detector is such that the count rate of the Ge detectors is 100 Hz, i.e., an event is recorded every tenth laser pulse, on average. Consider what will happen if some laser pulses generate ten times more x rays than the average laser pulse; this is a situation which does occur due to fluctuations of the experimental parameters. These pulses always produce a detected event, whereas other laser pulses may not produce any detectable hard x-ray radiation at all. The consequence of these large fluctuations is that the seemingly correct detection probability of 10% is in fact much higher for some pulses and pileup will occur in the detector. Therefore, the use of the NaI detector and the discriminator (see earlier) is important. The NaI signal monitors the total x-ray energy from each laser pulse and can be used to record the energy fluctuations on a pulse-to-pulse basis. The discriminator allows x-ray bursts with too high or too low energy, relative to a predefined energy window in the intensity gate, to be discarded. The NaI signal is not calibrated to the true x-ray intensity, but choosing a sufficiently small discriminator window, ensures that the true detection probability is close to the apparent one for all pulses. This is because with the use of the intensity gate, the detection probability can be calculated accurately, as the ratio between the number of photon events from the Ge detectors which is registered in the MCAs and the total number of pulses within the discriminator window, which is registered by a pulse counter.

Therefore, before a spectrum can be acquired, the upper and lower levels of the electronic discriminator are tuned to the x-ray intensity range to be investigated. Subsequently, suitable lead apertures are chosen for the germanium detectors. Acquisition is started and stopped after a few seconds and the detection probability of both detectors is evaluated.

The lead apertures are changed if necessary based on these results and the procedure is repeated until the desired detection probability is obtained.

To demonstrate the radiographic quality that can be achieved with this x-ray source, image plates (Fuji ST-VA) were employed.[33] An image plate is characterized by its linear response to x-ray exposure and its large dynamic range of four orders of magnitude. The active substance consists of small crystal fragments of a photosensitive phosphor layer. When the crystals are subject to ionizing radiation, electrons are excited and trapped in color centers. Subsequent readout with a focused red laser beam scanning over the plate produces fluorescence light, the intensity of which is proportional to the x-ray exposure. The image plates in this experiment were processed at the Lund University Hospital with Fuji image plate readers (FCR-5000). The system resolution is 5 pixels/mm and the matrix size 1760×2140 pixels. The Fuji system is roughly calibrated to the x-ray exposure, a quantity that can be measured with ion chambers or solid-state detectors. With an x-ray tube spectrum of 80 kV, filtered below 10 keV, exposures within the range of 0.01–10 mR can be converted into image data. This corresponds to a range of absorbed dose in air from 0.09 to 90 μGy. The exposure calibration is therefore sensitive to the x-ray spectrum, and since laser-produced x rays extend to higher energies, the calibration for this spectrum is different. Normally, the image plate processing unit automatically chooses which section of the total dynamic range of the image plate data is to be used to generate the final processed, digital image. It is, however possible, as was done in this experiment, to override this system in an external workstation and manually control the conversion to a digital image. The digital data are finally exported as 8-bit bitmap images. In the experimental setup, a lead brick arrangement served the purpose of keeping the image plate in place 0.7 m from the laser-produced plasma during exposure as, illustrated in Fig. 2. The object to be imaged, in this case a sacrificed Wistar–Furth rat held in place between two large, 6-mm-thick sheets of plexiglas, is placed against the image plate. The image plate is quite large, 35×43 cm^2, and each image requires only half the plate; the other half being shielded by lead.

V. THEORY

The conversion of the raw MCA (detector) spectra to laser-plasma emission spectra involves several steps and the resulting spectra have features that cannot easily be identified without some theoretical arguments. The results of the simulations described here are presented in the next section and they do, indeed, support the experimental findings. Apart from transmission, solid angle and detector efficiency, more intricate interactions such as Compton scattering and pileup must be included in the analysis; see Fig. 4. The latter interactions are only coarsely treated here but the theory still successfully describes their corresponding spectral features.

The starting point of the calculation is the hypothesis that the electron energy distribution in the laser plasma can be parameterized by a set of (three-dimensional) Maxwell distributions, the motivation for which can be found in the
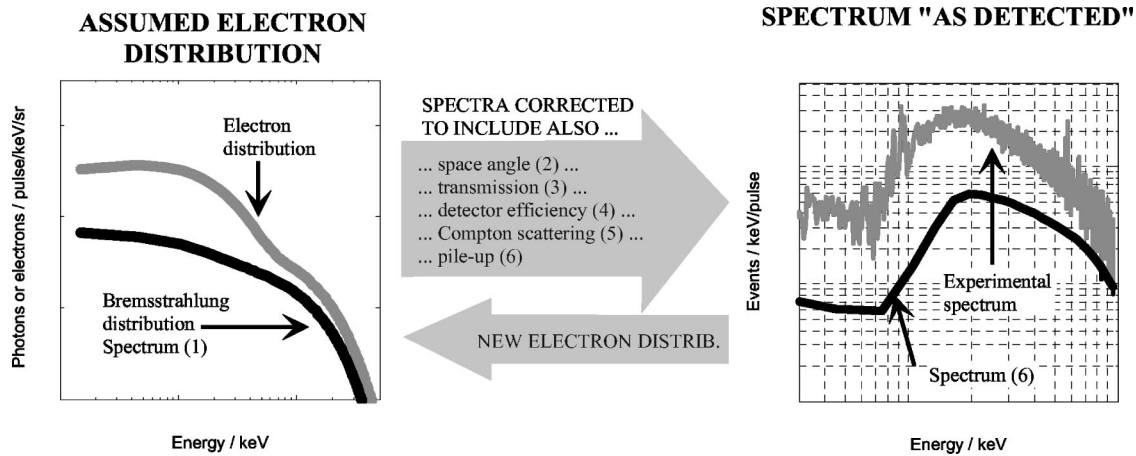
FIG. 4. The simulation process produces spectra with different levels of correction (1)–(6). The final spectrum (6) is compared with the raw spectrum data from the detector. The electron distribution is manually altered according to the visual comparison and the theoretical spectrum is recalculated. The process only requires a few iterations before a good fit to the experimental data is found. The simulations are performed for both detectors in parallel.

literature.[4,23,24,34] The tantalum target (atomic number Z) is subjected to the assumed electron energy distribution, $f(E_e)$ [1/keV], and generates a bremsstrahlung distribution, $g(E_B)$, which is modelled according to the expression[35,36]

$$g(E_B) \approx 2 \times 10^{-6} \times Z \times \int_{E_B}^{\infty} f(E_e)(E_e/E_B$$

$$-1)dE_e \quad (1/\text{keV}). \tag{1}$$

The bremsstrahlung photon energy is E_B and the electron energy is E_e, both measured in units of kilo-electron-volts. The characteristic radiation is a minor feature in the spectrum and it is disregarded here. Calculating the bremsstrahlung spectrum produces spectrum (1) in Fig. 4, and the subsequent calculations will be discussed in the order listed in the upper arrow in Fig. 4. Spectra (2)–(6), successively corrected for the processes listed, are detector dependent, and each step of the calculation is performed separately on the LEGe spectrum and the HPGe spectrum. The bremsstrahlung

spectrum is assumed to radiate isotropically, and only a small fraction of the x rays reach the detector through the lead aperture (2). Spectrum (2) is multiplied by the calculated transmission to provide spectrum (3), and then by the interpolated detector efficiency in Fig. 3 to give spectrum (4). In order to clarify the successive contributions to the spectrum, Fig. 5 shows spectra (2), (3), and (4).

The detector efficiencies are small at low energies because the photons are unable to reach the active region of the germanium crystal as they are absorbed on the way. The low detector efficiencies at high energies are due to the low cross section for photoelectric absorption in germanium. The probability of Compton scattering, however, is large. It is possible to make a crude estimate of the Compton background based on a few simple arguments. First, a modified spectrum (3) is employed to calculate the amount of Compton scattering: the photons that will be detected according to the intrinsic full-energy-peak efficiency are subtracted from spectrum
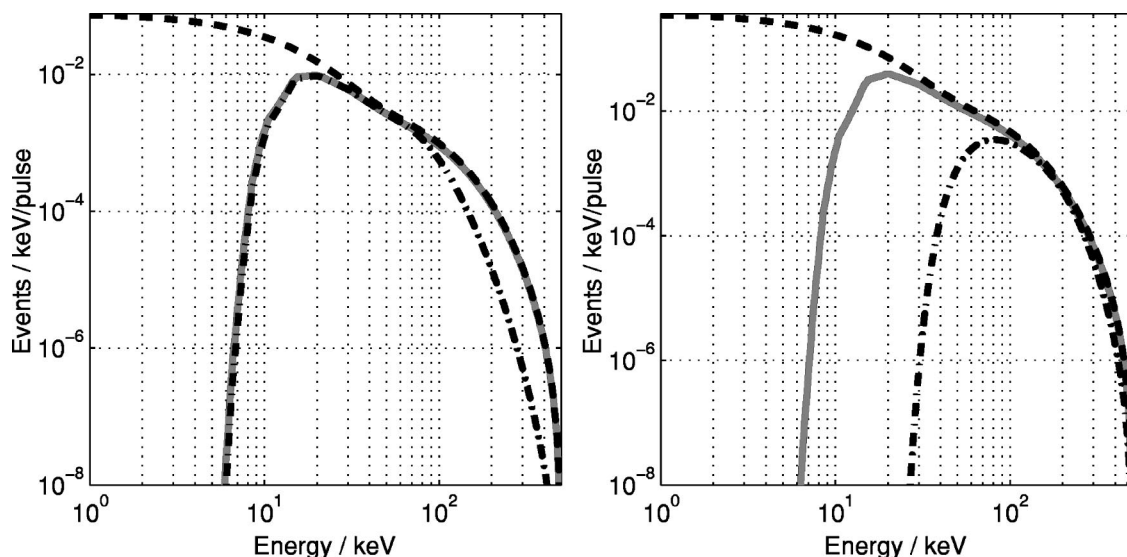

FIG. 5. Spectra (2), (3), and (4) for both detectors. Spectrum (2) (dashed) is the calculated bremsstrahlung spectrum scaled by the solid angle. Spectrum (3) (solid) includes the transmission to the detector, and spectrum (4) (dash-dot) also includes the intrinsic full-energy-peak efficiency of the detector. Thus, spectrum (4) represents the photons that reach the detector and deposit all their energy.

(3). The resulting spectrum is an assessment of the photons that may be Compton scattered before leaving the detector. Second, the energy distribution of the Compton events is assumed to be flat, as in Fig. 6, starting at zero energy and extending up to $E_C = E/1 + 256/E$ where E is the energy in kilo-electron-volts of a photon that is Compton scattered. A better-estimate of the Compton energy distribution can be obtained from the theory of Klein and Nishina,[37] but this adds to the complexity without changing the fundamental features of the resulting Compton background significantly. Finally, theoretical cross sections from NIST are used to calculate the absolute number of photons that are Compton scattered once.[32] Multiple Compton scattering is bound to occur, and is probable, but a theoretical description would require a full Monte Carlo simulation, which is beyond the scope of this study. Refer to Sec. VI for a discussion on the effects of multiple scattering. The Compton events obtained form a background which is added to spectrum (4) giving a spectrum with the Compton background (5).

Calculating how pileup affects the spectrum is somewhat more complicated. The spectrum, dn/dE, is treated as a discrete distribution with discretization size ΔE. The number of events, $n_E = (dn/dE)\Delta E$, at an x-ray energy, E, is assumed to be Poisson distributed, $n_E \in Po(\bar{N}_E)$. The average number of x-ray photons (at energy E) per pulse that enter the detector is $\bar{N}_E$; given by the Compton spectrum (5). Consequently, the probability of measuring only a single photon at energy E_x, in one laser pulse, is expressed by

$$p_1(E_x) = P(n_{E_x} = 1) \times \prod_{E \neq E_x} P(n_E = 0). \qquad (2)$$

The probability of measuring two photons with the total energy E_x is

$$p_2(E_x) = \sum_{E_1 + E_2 = E_x} \left[P(n_{E_1} = 1) \times P(n_{E_2} = 1) \right. $$
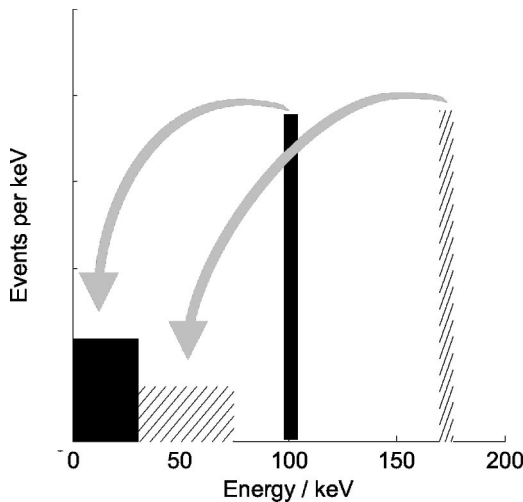$$\left. \times \prod_{E \neq E_1, E_2} P(n_E = 0) \right], \qquad (3)$$

FIG. 6. Illustration of how photons with two different energies produce different Compton electron distributions.

and that of measuring three photons with the total energy E_x:

$$p_3(E_x) = \sum_{\substack{E_1 + E_2 + E_3 = E_x \\ E_1 \neq E_2 \neq E_3}} \left[P(n_{E_1} = 1) \times P(n_{E_2} = 1) \right.$$
$$\left. \times P(n_{E_3} = 1) \times \prod_{E \neq E_1, E_2, E_3} P(n_E = 0) \right]$$
$$+ \sum_{\substack{2 \times E_1 + E_2 = E_x \\ E_1 \neq E_2}} \left[P(n_{E_1} = 2) \times P(n_{E_2} = 1) \right.$$
$$\left. \times \prod_{E \neq E_1, E_2} P(n_E = 0) \right] + \sum_{3 \times E_1 = E_x} \left[P(n_{E_1} = 3) \right.$$
$$\left. \times \prod_{E \neq E_1} P(n_E = 0) \right], \qquad (4)$$

and so on. This reasoning reduces to the total probability of detecting a photon or a sum of photons of energy E_x, in one laser pulse

$$p_{\text{total}}(E_x) = \sum_{i=1}^{\infty} p_i(E_x). \qquad (5)$$

In practice it is sufficient to consider only two- or three-photon pileup if the detection probability per pulse is around 10%.

When the Compton spectrum (5) has been modified for pileup, the spectrum obtained, spectrum (6), should correspond to the raw Ge detector spectrum as it appears in the MCA. Typical examples of spectra (4), (5), and (6) are shown in Fig. 7. Spectrum (6) is compared with the experimental spectrum and the initial electron distribution is manually modified and a new round of calculations is performed until the simulated spectra agree well with both experimental detector spectra. At this point, when the agreement between the simulated and the detected spectra is optimal, the simulated bremsstrahlung spectrum represents the plasma emission spectrum.

VI. EXPERIMENTAL AND SIMULATED X-RAY SPECTRA

Typical Ge detector spectra are presented in Figs. 8(a) (LEGe) and 8(b) (HPGe). The acquisition time was 11 min ($\sim 7 \times 10^5$ laser pulses). The gray traces are the experimental findings as they appear in the MCAs of the two detectors. The LEGe data extend up to 95 keV, while the HPGe data extend up to 0.5 MeV. These energy limits are determined by the MCA settings. Thus, neither of the detector spectra can fully describe the true emission spectrum, but together they determine the parameters for the best simulation. Three simulated spectra are also shown for each detector. The dashed trace is spectrum (4) which, as expected, contains almost no events below 7 keV. The dotted trace, which sometimes overlaps the solid, black trace, represents spectrum (5), i.e., including the Compton background. Finally, the solid, black trace corresponds to spectrum (6), which includes two- and three-photon pileup. The lead apertures in front of the
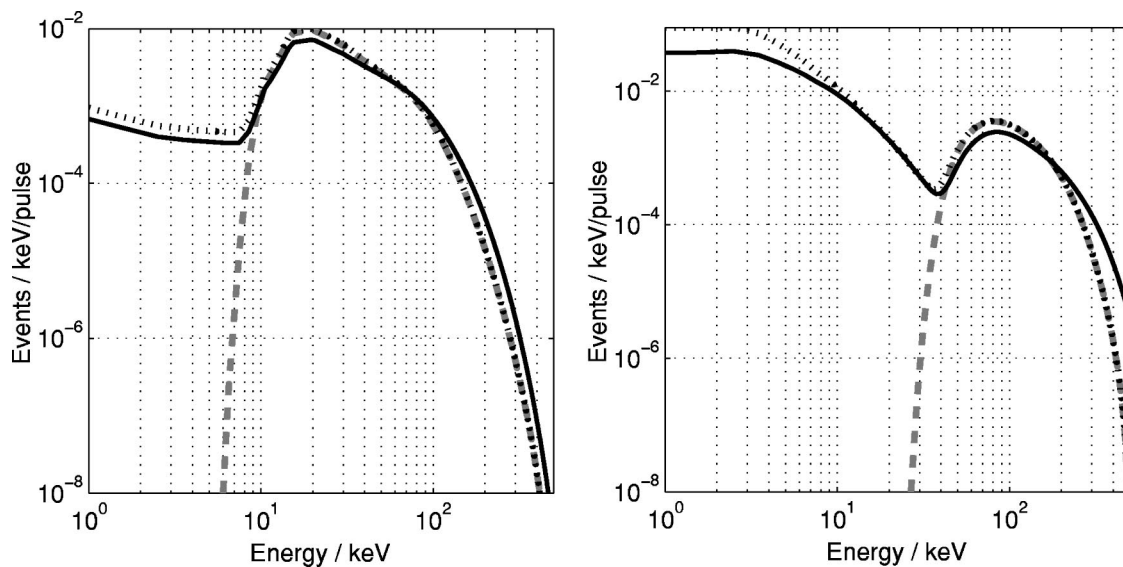
FIG. 7. The simulated spectra (4), (5), and (6) for both detectors. Spectrum (4) (dashed) includes the solid angle correction, the transmission and the detector efficiency. Spectrum (5) (dotted), includes the Compton background and the solid trace. Spectrum (6) (solid), also includes the effect of pileup. The detection probability for each simulated laser pulse is 14% in this example.

Ge detectors were rather small during this acquisition (LEGe: ⊘ 3.5 mm, HPGe: ⊘ 11 mm) giving average detection probabilities of the order of 10%. It is clear that pileup modifies the high-energy tail of the HPGe spectrum, even when the detection probability is this low [Fig. 8(b)]. The intensity gate restricts pulse-to-pulse fluctuations of the x-ray yield to within a factor of 2. This acts as a precaution against very intense x-ray bursts and accepts 80% of the x-ray bursts. Spectrum (6) generally follows the experimental data in Fig. 8. The main discrepancies are between 30 and 80 keV for the HPGe detector [Fig. 8(b)] and below 10 keV for the LEGe detector [Fig. 8(a)] where the simulated spectrum underestimates the number of events. The probable reason for this is that the Compton background is underestimated at

these energies. In the case of the HPGe detector this is explained by the fact that the simulation includes no more than one Compton scattering event per photon which causes the Compton events have too low energy, on average. A photon that is scattered twice, for example, deposits more energy in the detector than it would if it were scattered only once. Because the probability for scattering occurring is more than 50% in the detectors, multiple scattering is probable. The number of Compton events does not increase with multiple scattering, but the distribution of events changes, effectively moving events from lower to higher energies. In the case of the LEGe detector, the underestimation can be explained by the large uncertainty in detector efficiency above 100 keV (cf. Fig. 3). The main contribution to the Compton back-
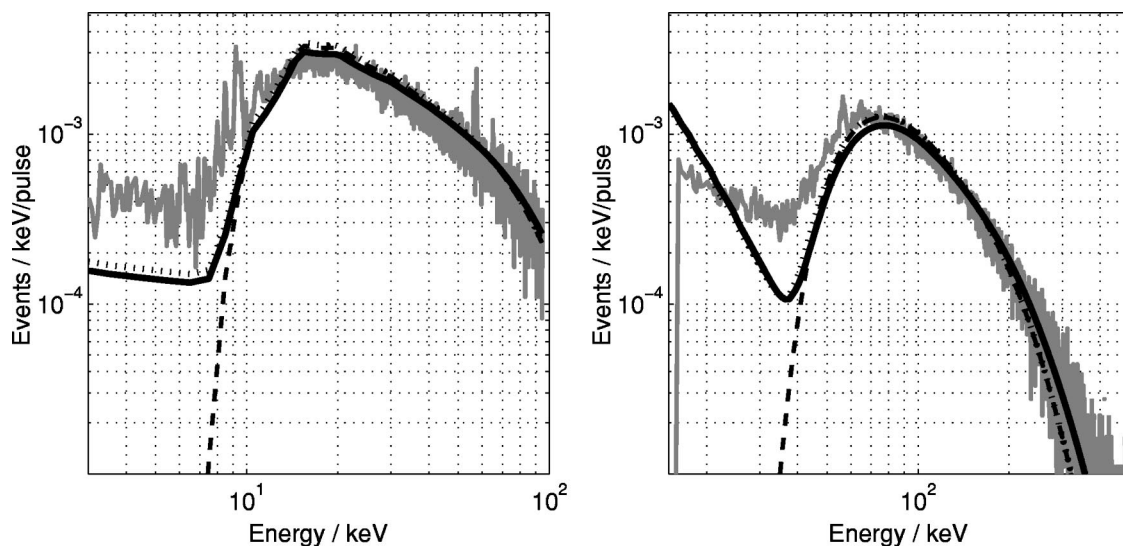

FIG. 8. Two experimental x-ray spectra (gray) as they appear in the MCA. The laser energy on the target was 0.7 mJ with a pulse duration of 25 fs 80%, or 5.4×10^5 pulses, was accepted by the discriminator. Also shown are simulated traces based on an electron distribution consisting of a sum of two Maxwellian distributions; 1.3×10^{10} electrons with a temperature of 4.5 keV and 1.6×10^8 electrons with a temperature of 63 keV. Referring to Fig. 4, the solid, black traces correspond to spectrum (6) and the dotted traces are similar but with pileup omitted. The dashed traces show the simulated spectra without Compton scattering and pileup. The two latter traces overlap at high energies.
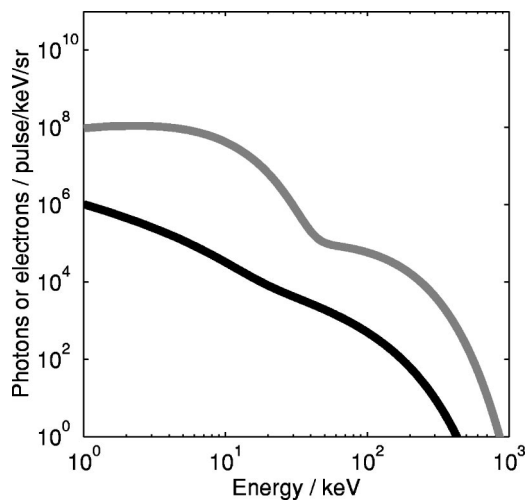
FIG. 9. The electron distribution function and laser-plasma emission spectrum based on the data in Fig. 8. The electron distribution is the upper trace with its corresponding bremsstrahlung spectrum below.
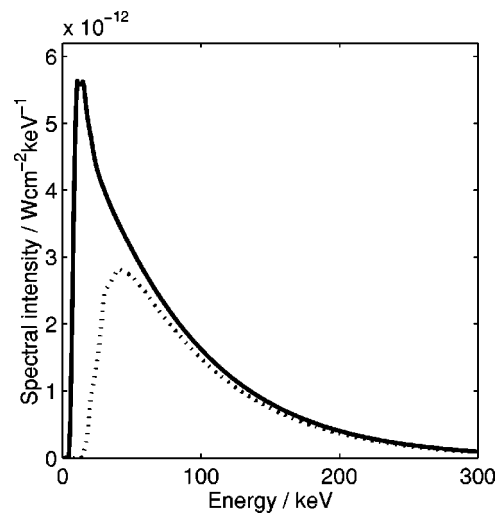

FIG. 11. The solid trace is the simulated average x-ray intensity distribution at 0.7 m from the plasma, where the image plate and the experimental animal are located. The electron distribution for the simulation is identical to that shown in Fig. 8. The intensity after passing through the object, the dotted trace, is calculated by modeling the animal as 2-cm-thick soft tissue between two sheets of 6-mm-thick plexiglass.

ground comes from these photons, which means that an error in the efficiency directly affects the level of the Compton background.

The theoretical electron distribution that gives the best fit between the calculated and measured spectra consists of two three-dimensional Maxwellian distributions; one with 1.3×10^{10} electrons with a temperature of 4.5 keV and the other with 1.6×10^8 electrons with a temperature of 63 keV, i.e., a factor of 100 between the number of electrons. The electron distribution is plotted in Fig. 9 as the gray trace. The plasma emission spectrum, i.e., the bremsstrahlung spectrum [spectrum (2)], is the black trace in the same figure.

The total energy, relative to the laser energy, is 2.4% for the earlier electron distribution and 6×10^{-4} for the bremsstrahlung emission. However, it is possible to add a third Maxwellian electron distribution with a low temperature, less than 1 keV, and a large number of electrons, without influencing the observed spectra. With a temperature of 1 keV the number of electrons can be increased to 3×10^{12}, corresponding to complete absorption of the laser pulse energy. In other words; such an electron distribution cannot be detected with the present choice of detectors.

It is difficult to evaluate the uncertainty of the solid angles, transmissions, and detector efficiencies, but the un-

certainty in the simulation itself is quite small; a single, unambiguous sum of electron Maxwell distributions match the data. The implication of this is discussed in physical terms below.

Figures 10(a) and 10(b) show magnified views from Fig. 8(a). They reveal the characteristic radiation emitted from the tantalum target. The LEGe detector almost resolves the two $L\beta$ peaks which are separated by only 0.3 keV. The fine structure of the $L\alpha$ emission is partly resolved.

VII. RESULTS FROM X-RAY IMAGING

The image plate with the object up against it is placed 0.7 m from the plasma. The simulated bremsstrahlung radiation shown in Fig. 9 predicts that the average x-ray intensity is 4 nW/cm² at this distance, integrated over the spectrum. The intensity distribution is plotted in Fig. 11. The dotted trace is the calculated intensity that reaches the image plate after passing through the thin glass debris shield, the window at the air-vacuum interface, 0.7 m air, 12 mm plexiglas and 20 mm soft tissue (the rat). The x-ray intensity has decreased
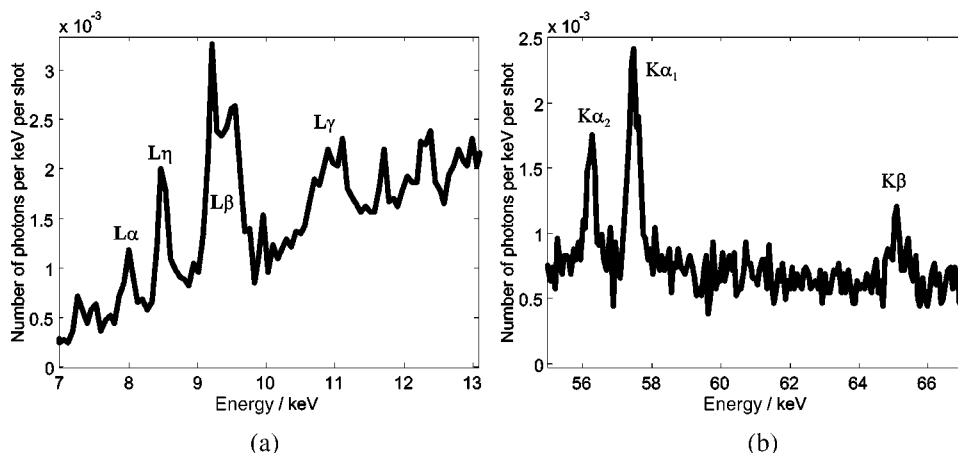

(a)

(b)

FIG. 10. (a) Magnified view of the LEGe spectrum in Fig. 8(a), showing the characteristic L radiation from tantalum. It is possible that the peak structures between 10.5 and 13 keV are caused partly by L radiation from the lead aperture in front of the detector. (b) Magnified view of the LEGe spectrum in Fig. 8 (a), showing the characteristic K radiation from tantalum.
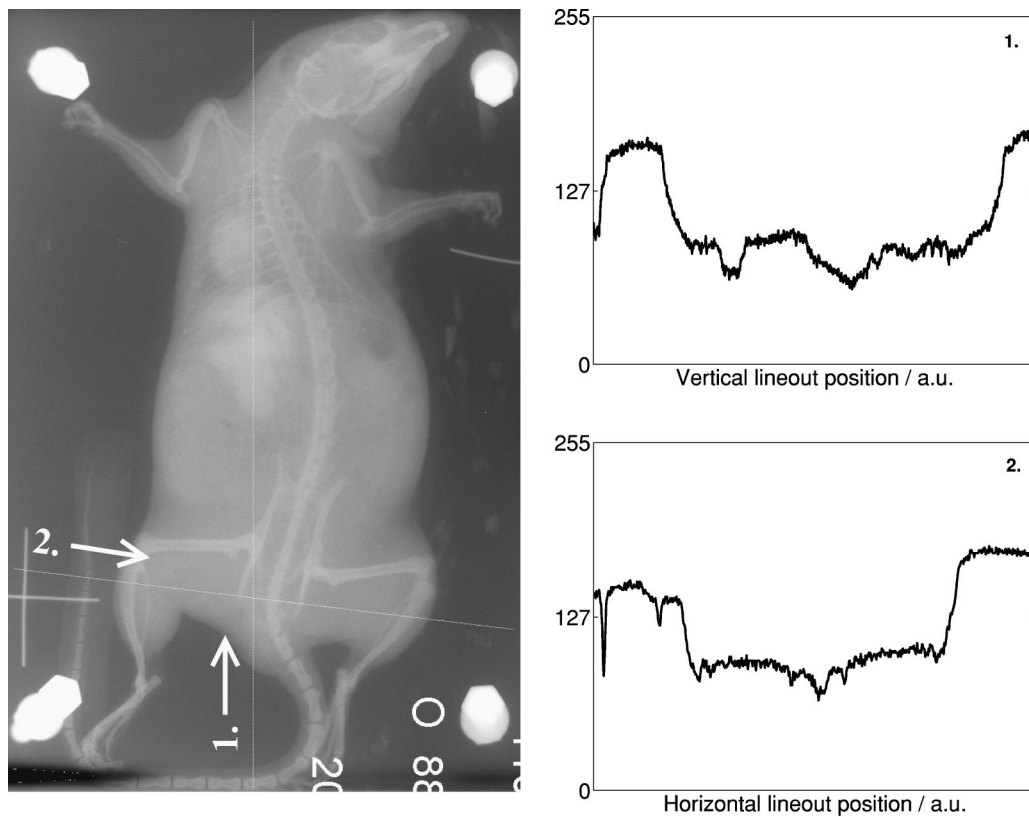
FIG. 12. To the left is a 5 min exposure of a sacrificed Wistar–Furth rat, 0.7 m from the laser plasma (the image is 20 cm high). The greyscale extends from 7 (white) to 36 μGy (black). The cross in the lower, left corner of the rat image is the image of a platinum wire, 0.5 mm in diameter. It was used to determine whether the object had moved accidentally during the exposure, and also to indicate the amount of scattering in the object. The right part of the figure shows the vertical and horizontal line-out traces, as indicated in the rat image.

to 3 nW/cm^2, with the x rays from 30 to 150 keV primarily contributing to the exposure. The photons in this energy range are exclusively produced by the 63 keV electron distribution.

The rat images in Figs. 12, 13, and 14 have been processed with the Fuji image plate system. The scales for the absorbed dose used in the images are based on the calibration with an 80 keV x-ray tube spectrum. This calibration is believed to underestimate the dose arising from the laser-plasma spectrum by roughly a factor of 2. Figure 12 for example, include levels of absorbed dose from 7 (white) to 36 μGy (black) in steps of 0.1 μGy. The average dose of the pixels in the rat is 17 μGy, which can be related to the average x-ray intensity incident on the image plate. The relation depends on the x-ray energy absorbed per unit mass in air and in the image plate. The absorption coefficients vary with the x-ray energy, but if the x-ray spectrum extends from 30 keV and upwards, such as in the case of the object-transmitted x rays in Fig. 11, the variations are not large. Using the fact that the exposure time for the rat in Fig. 12 is 5 min, the dose suggests an average x-ray intensity of 2 nW/cm^2, in very good agreement with the predicted value. This confirms the assumptions made regarding the exposure levels of the image plates are valid.

The image plate contrast is manifested by the line-out traces in Fig. 12. The perceived contrast is simply a matter of the settings of the Fuji device used to process the image plate data, as the signal-to-noise ratio is very high in this image.

The perceived contrast, as evaluated in this image, is about 0.25 between bone and soft tissue and 0.5 between the rat and its surroundings. However, since "zero" signal in Fig. 12 corresponds to 7 μGy absorbed dose in air, the values of the true contrast is only 0.13 and 0.35. The contrast for small objects, such as the platinum wire (Fig. 12), which is only 0.5 mm thick, may be degraded by scattering in the surrounding material.

Figure 13 shows a rat exposed for 1 min. At first glance, the contrast may be perceived to be better in this image. However, the image is more grainy than the 5 min exposure image, indicating the lower dose. The actual signal-to-noise ratio is worse than in the 5 min exposure (Fig. 12), but still good enough for many diagnostic purposes. The bone tissue, for example, can be well discerned.

The quality deteriorates as the image exposure approaches the lowest possible value for the image plate system. A 10 s exposure is presented in Fig. 14. In this case, the lowest level of absorbed dose (white) corresponds to only 0.8 μGy. Not even the solid bones give a good contrast in this image. The image is grainy because of the low dose and the contrast deterioration is due to the low signal-to-noise ratio. The dynamic range of the dose in Figs. 12, 13, and 14 does not linearly scale with the exposure time. This is explained by the limited dynamic range of the image plates employed. The dynamic ranges have been chosen to give a good visibility in print.

FIG. 13. A 1 min exposure of a sacrificed Wistar–Furth rat. The greyscale extends from 2 (white) to 13 μGy (black) over 256 levels.

FIG. 14. Image plate recording of the same object as in Figs. 12 and 13, but with only 10 s exposure time. The greyscale extends from 0.8 (white) to 4 μGy (black).

VIII. DISCUSSION

The calculations suggest a bi-Maxwellian electron distribution causing the bremsstrahlung spectrum to reproduce the dual-temperature feature that is experimentally measured. It can be excluded that the two temperatures (4.5 and 63 keV) originate from random ''good and bad'' pulses, because these can be identified via accompanying large x-ray intensity fluctuations, and the intensity gate controls the sampling.

It is generally agreed on in the literature that the resonance heating of electrons generates a hot electron distribution, in many cases similar to one or several Maxwell distributions.[4,34] The corresponding hot temperatures scale as $T_{\text{hot}} \propto (I\lambda^2)^{0.33}$, where λ and I are the laser wavelength and intensity.[23,24,38,39] However, the exact expression for the temperature depends on many more factors, such as the temperature of the electrons in the overdense plasma region and the scale length of the plasma.[39] In the present investigation, the laser intensity was estimated through a series of reasonable assumptions leading to a lower limit of 10^{16} W/cm^2. Applying the earlier scaling to the results reported by Beg *et al.*,[38] resonance heating is expected to produce a temperature in the region of 45 keV with our laser parameters. The results presented by Pretzler *et al.* indicate that resonance heating can generate two temperatures,[4] and with the scaling earlier, those temperatures may be $\sim$7 and 63 keV if an intensity of 6×10^{16} W/cm^2 is used. Applying this intensity instead to the scaling of Beg *et al.*, results in an electron temperature of 76 keV. Therefore, our temperature of 63 keV agrees quite well

with those measured by others. The lower temperature of 4.5 keV, could be caused by vacuum heating, but a condition for this mechanism is that the plasma density gradient is sharp. Such a sharp gradient requires that there is no pre-ionization and no early pre-plasma,[21,23,34,39] a situation which could apply to this experiment considering the intensity and the prepulse contrast. However, the rather low laser intensity is probably insufficient to be able to heat the plasma electrons sufficiently through this process. Furthermore, the lower temperature in particular should be considered very approximate, bearing in mind the energy range of the detectors.

The x-ray spectrum in Fig. 11 resembles an x-ray tube spectrum with the voltage set at around 300 kV. Only the 63 keV electron distribution produces x rays that are useful for medical imaging with the image plates ($>$20 keV), while the x rays from the 4.5 keV electron distribution are filtered away. Medical x-ray diagnostics is usually performed with tube voltages in the range from 27 to 140 kV. The lower x-ray energies are used to maximize the image contrast in soft tissue (e.g., mammography), while the highest voltage is needed for lung examinations. Voltages above 150 kV are not applied; a result of the compromise between the image quality and the patient dose, which also explains why soft x rays below 10 keV are normally filtered away. With other laser systems, with higher peak focused intensity, it is possible to heat the plasma to much higher temperatures than in the present study, but from a medical imaging point of view, as the results from the imaging show, this is not desirable.

The plasma temperature should not exceed ~50 keV but the average x-ray flux should be increased instead.

Concluding the discussion, we have shown that with 25 fs laser pulses of less than 1 mJ of energy, the x-ray radiation spectrum from the laser plasma is not unlike that generated by more energetic laser pulses, with a few discrete electron temperatures due to different heating mechanisms. The fact that the highest electron temperature is less than 50 keV is advantageous in many applications where radiation above 100 keV is undesirable. The image plates work well with an absorbed dose (in air) around 4 μGy, which in this experiment corresponds to a 1 min exposure at a relatively large distance of 0.7 m. This might be too long a time for practical purposes, but there are many ways of optimizing the conditions. The distance to the source can easily be reduced and the energy in the laser pulses can be increased by almost an order of magnitude with existing laser technology, allowing a larger focal volume while maintaining the intensity in the region of 10^{16} W/cm^2. Together, these changes can easily reduce the exposure time to only a few seconds. Furthermore, with new laser systems with repetition rates of tens of kilohertz presently coming into use, it is plausible that the required exposure time can be reduced to less than a second in the near future. Moreover, the laser-produced x rays have the great advantage of coming in very short bursts ($\lesssim$10 ps). This enables gated viewing, which has the potential of decreasing the patient dose without causing deteriorating of the contrast in the diagnostic images.[40] Thus, the combination of the readily achievable realistic exposure times and the gated viewing technique clearly motivates more investigations in this area.

ACKNOWLEDGMENTS

[1] J. D. Kmetec, C. L. Gordon, J. J. Macklin, B. E. Lemoff, G. S. Brown, and S. E. Harris, Phys. Rev. Lett. **68**, 1527 (1992).

[2] K. Herrlin, G. Svahn, C. Olsson, H. Petterson, C. Tillman, A. Persson, C.-G. Wahlström, and S. Svanberg, Radiology **189**, 65 (1993).

[3] H. Schwoerer, P. Gibbon, S. Dusterer, R. Behrens, C. Ziener, C. Reich, and R. Sauerbrey, Phys. Rev. Lett. **86**, 2317 (2001).

[4] G. Pretzler, T. Schlegel, E. Fill, and D. Eder, Phys. Rev. E **62**, 5618 (2000).

[5] G. Kulcsár, D. AlMawlawi, F. W. Budnik, P. R. Herman, M. Moskovits, L. Zhao, and R. S. Marjoribanks, Phys. Rev. Lett. **84**, 5149 (2000).

[6] J. Yu, Z. Jiang, J. C. Kieffer, and A. Krol, Phys. Plasmas **6**, 1318 (1999).

[7] C. Y. Cote, J. C. Kieffer, Z. Jiang, A. Ikhlef, and H. Pepin, J. Phys. B **31**, L883 (1998).

[8] A. Ikhlef, Z. Jiang, J. C. Kieffer, and A. Krol, J. X-Ray Sci. Technol. **8**, 151 (1998).

[9] Y. Jiang, T. W. Lee, W. Li, G. Ketwaroo, and C. G. Rose-Petruck, Opt. Lett. **27**, 963 (2002).

[10] E. Andersson, G. Hölzer, E. Förster, M. Grätz, L. Kiernan, A. Sjögren, and S. Svanberg, J. Appl. Phys. **90**, 3048 (2001).

[11] G. Hölzer, E. Förster, M. Grätz, C. Tillman, and S. Svanberg, J. X-Ray Sci. Technol. **7**, 50 (1997).

[12] N. Takeyasu, Y. Hirakawa, and T. Imasaka, Appl. Phys. Lett. **78**, 1195 (2001).

[13] L. M. Chen *et al.*, Phys. Rev. Lett. **87**, 225001 (2001).

[14] Q. L. Dong, J. Zhang, and H. Teng, Phys. Rev. E **64**, 026411 (2001).

[15] P. Zhang *et al.*, Phys. Rev. E **57**, R3746 (1998).

[16] G. Jennings, W. J. H. Jager, and L. X. Chen, Rev. Sci. Instrum. **73**, 362 (2002).

[17] C. Tillman, S. A. Johansson, B. Erlandsson, M. Grätz, B. Hemdal, A. Almén, S. Mattsson, and S. Svanberg, Nucl. Instrum. Methods Phys. Res. A **394**, 387 (1997).

[18] M. Grätz, Ph.D. thesis, Lund Institute of Technology, LRAP-236, 1998.

[19] K. Herrlin, C. Tillman, M. Grätz, C. Olsson, H. Pettersson, G. Svahn, C.-G. Wahlström, and S. Svanberg, Interface (Netherlands) **32**, 306 (1997).

[20] C. Tillman, Ph.D. thesis, Lund Institute of Technology, LRAP-204, 1996.

[21] T. Schlegel *et al.*, Phys. Rev. E **60**, 2209 (1999).

[22] F. Brunel, Phys. Rev. Lett. **59**, 52 (1987).

[23] K. Estabrook and W. L. Kruer, Phys. Rev. Lett. **40**, 42 (1978).

[24] D. W. Forslund, J. M. Kindel, and K. Lee, Phys. Rev. Lett. **39**, 284 (1977).

[25] P. P. Rajeev, S. Banerjee, A. S. Sandhu, R. C. Issac, L. C. Tribedi, and G. R. Kumar, Phys. Rev. A **65**, 052903 (2002).

[26] U. Teubner, J. Bergmann, B. V. Wonterghem, F. P. Schäfer, and R. Sauerbrey, Phys. Rev. Lett. **70**, 794 (1993).

[27] R. Fedosejevs, R. Ottmann, R. Sigel, G. Kühnle, S. Szatmari, and F. P. Schäfer, Phys. Rev. Lett. **64**, 1250 (1990).

[28] M. Grätz, C. Tillman, I. Mercer, and S. Svanberg, Appl. Surf. Sci. **96**, 443 (1996).

[29] G. Korn, A. Thoss, H. Stiel, U. Vogt, M. Richardson, T. Elsaesser, and M. Faubel, Opt. Lett. **27**, 866 (2002).

[30] D. von der Linde, K. Sokolowski-Tinten, C. Blome, C. Dietrich, A. Tarasevitch, A. Cavalleri, and J. A. Squier, AIP Conf. Proc. **611**, 63 (2002).

[31] C. Rose-Petruck *et al.*, Nature (London) **398**, 310 (1999).

[32] M. J. Berger, J. H. Hubbell, S. M. Seltzer, J. S. Coursey, and D. S. Zucker, Tech. Rep., National Institute of Standards and Technology, 1999, URL http://physics.nist.gov/xcom.

[33] J. Miyahara, Chem. Today **223**, 29 (1989).

[34] W. L. Kruer, *The Physics of Laser Plasma Interactions* (Addison-Wesley, New York, 1988).

[35] M. Lamoureux, P. Waller, P. Charles, and N. B. Avdonina, Phys. Rev. E **62**, 4091 (2000).

[36] G. H. McCall, J. Phys. D **15**, 823 (1982).

[37] R. D. Evans, *The Atomic Nucleus* (McGraw-Hill, New York, 1955).

[38] F. N. Beg *et al.*, Phys. Plasmas **4**, 447 (1996).

[39] P. Gibbon and E. Förster, Plasma Phys. Controlled Fusion **38**, 769 (1996).

[40] M. Grätz, L. Kiernan, C.-G. Wahlström, S. Svanberg, and K. Herrlin, Appl. Phys. Lett. **73**, 2899 (1998).